Supporting Information

A combined experimental and computational approach reveals how aromatic peptide amphiphiles self-assemble to form ion-conducting nanohelices

Yin Wang [1,#], Yaxin An [2,#], Yulia Shmidov[3], Ronit Bitton [3], Sanket A. Deshmukh [2,*], John B. Matson [1,*]

[1] Department of Chemistry, Virginia Tech Center for Drug Discovery, and Macromolecules Innovation Institute, Virginia Tech, Blacksburg, VA 24061, United States. Email: jbmatson@vt.edu

[2] Department of Chemical Engineering, Virginia Tech, Blacksburg, VA 24061, United States. Email: sanketad@vt.edu

[3] Department of Chemical Engineering and the Ilze Katz Institute for Nanoscale Science and Technology, Ben-Gurion University of the Negev, Beer-Sheva 84105, Israel

# These authors contributed equally to this work.

Table of Contents

Materials

All Fmoc amino acids and Rink amide MBHA resin were purchased from Peak Polypeptide Biosystems LLC (P3BioSystems, Louisville, KY, USA). 4-Formylbenzoic acid (FBA) was purchased from Chem-Impex International, Inc (Wood Dale, IL, USA). *O*-Benzylhydroxylamine hydrochloride, thiobenzoic acid, deoxyribonucleic acid from herring sperm, and poly(sodium 4-styrene-sulfonate) (PSSS, M_w ~1,000,000) were purchased from Sigma-Aldrich (St. Louis, MO, USA). Poly(acrylic acid) sodium salt (PAA, M_w ~6,000) was purchased from Polysciences, Inc (Warrington, PA, USA). Alginic acid sodium salt was purchased from RPI Research Products International (Mount Prospect, IL, USA). All other reagents were sourced from Sigma-Aldrich (St. Louis, MO) or VWR (Radnor, PA, USA), unless otherwise stated. *S*-Benzoylthiohydroxylamine (SBTHA) was synthesized according to our previous report.[1]

Peptide synthesis

All peptides used in this study were manually synthesized using standard 9-fluorenylmethoxycarbonyl (Fmoc) solid phase synthesis techniques at a 0.5 mmol scale. Fmoc deprotection steps were carried out by treating the Rink amide MBHA resin with 4-methylpiperidine in dimethylformamide (DMF) (20% v/v). Amino acid coupling steps were performed following Fmoc deprotection by treating the resin with Fmoc-amino acid, *O*-benzotriazole-*N,N,N′,N′*-tetramethyluronium hexafluorophosphate (HBTU), and diisopropylethylamine (DIEA) (4:3.96:10 molar ratio to amine groups on resin) in DMF for 2 h. After coupling of the final amino acid, removal of the Mtt protecting group derived from Fmoc-Lys(Mtt)-OH was achieved by treating the resin with trifluoroacetic acid (TFA)/triisopropylsilane (TIS)/DCM (3:5:92). FBA was then coupled to the Lys ε-amine using the same coupling conditions as noted above for Fmoc amino acids. The final Fmoc group was then removed, and the *N*-terminus was acetylated by treating the resin with a mixture of acetic anhydride (10 mL, 20% in DMF) and DIEA (80 μL) three times. Finally, peptides were cleaved from the resin by treatment with a TFA/H_2O (97.5:2.5) solution (15 mL) for 3 h. The solution was concentrated in vacuo and triturated with cold diethyl ether to precipitate the crude peptide. Following centrifugation to remove the supernatant liquid, the crude materials were dissolved in the mixture of water and acetonitrile containing 0.1% NH_4OH for purification.

All peptides were purified by preparative RP-HPLC using an Agilent Technologies 1260 Infinity HPLC system (Agilent Technologies, Santa Clara, CA) equipped with a fraction collector. Separations were performed using an Agilent PLRP-S column (100 Å, 10 μm, 150 × 25 mm) monitoring at 220 nm. The expected mass was confirmed using ESI-MS (Advion ExpressIon Compact Mass Spectrometer). Fractions containing pure products were combined and lyophilized (FreeZone −105 °C, Labconco, Kansas City, MO), and then stored at −20 °C.

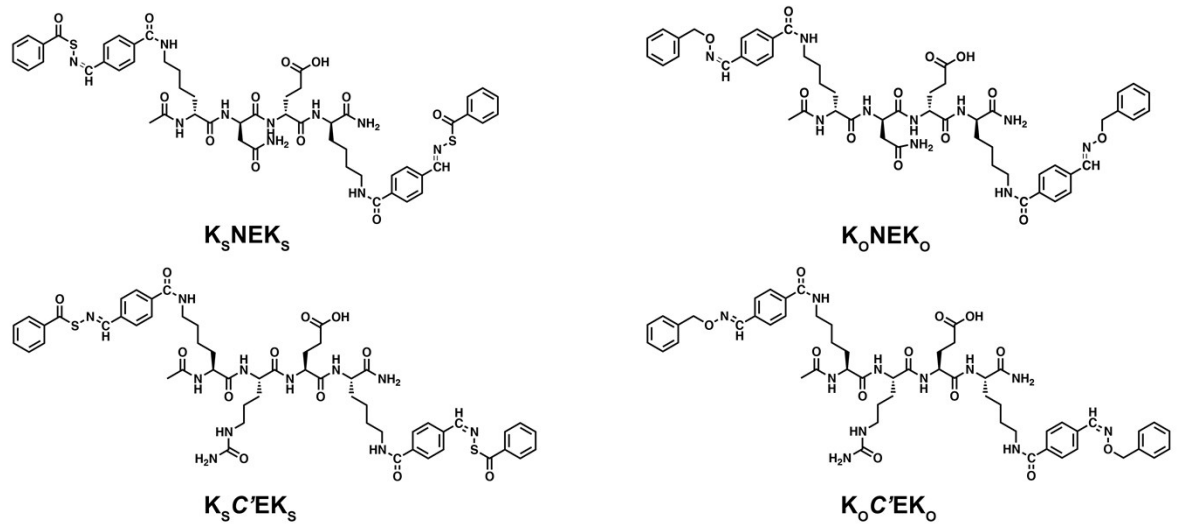

Fig. S1 Molecular structures of all APAs and the control APAs studied here.

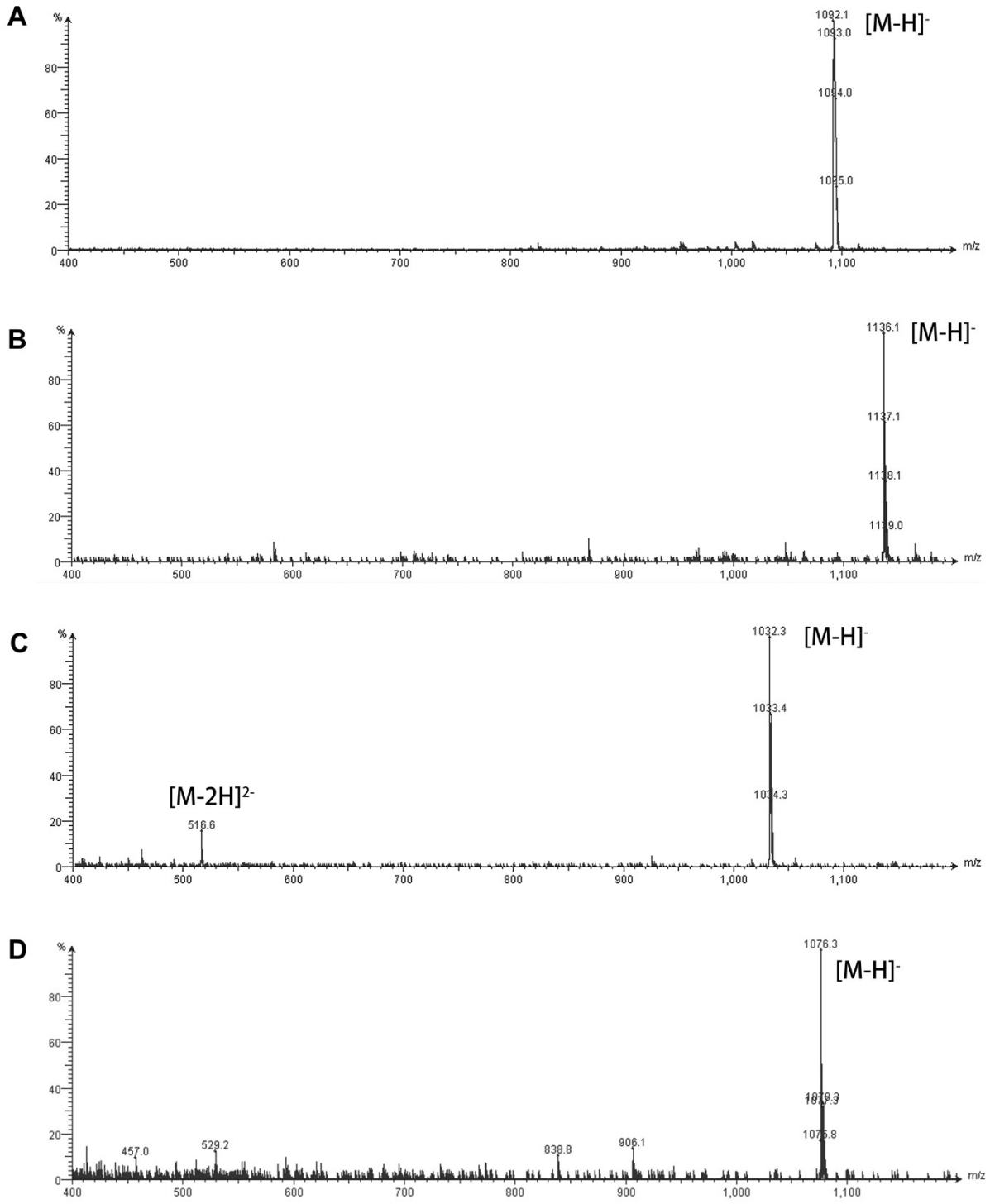

Fig. S2 ESI mass spectra of (A) $\mathbf{K_SNEK_S}$, (B) $\mathbf{K_S}\boldsymbol{C'}\mathbf{EK_S}$, (C) $\mathbf{K_ONEK_O}$, and (D) $\mathbf{K_O}\boldsymbol{C'}\mathbf{EK_O}$.

Characterization of self-assembled APAs

Conventional transmission electron microscopy (TEM):

1 mM stock solutions of APAs in 10 mM or 100 mM phosphate buffer (PB) solution (pH 7.4) were prepared by direct dissolution of the lyophilized powders. Samples were allowed to age overnight. An aliquot of each solution was removed immediately prior to TEM sample preparation and diluted with 10 mM or 100 mM PB to 100 μM. Next, 10 μL of this solution was deposited on a carbon-coated copper grid (Electron Microscopy Services, Hatfield, PA, USA) and allowed to stand for 5 min. Excess solution was wicked away by a small piece of filter paper, and then DI water was deposited, allowed to stand for 40 sec, and then wicked away to wash away excess salts. Finally, 10 μL of a 2 wt % aqueous uranyl acetate (UA) solution was deposited on the grid for 5 min. A thin layer was generated after carefully wicking away excess UA. The sample grid was then allowed to dry at rt prior to imaging. Bright-field TEM imaging was performed on a Philips EM420 TEM operated at an acceleration voltage of 100 kV. TEM images were recorded by a slow scan CCD camera.

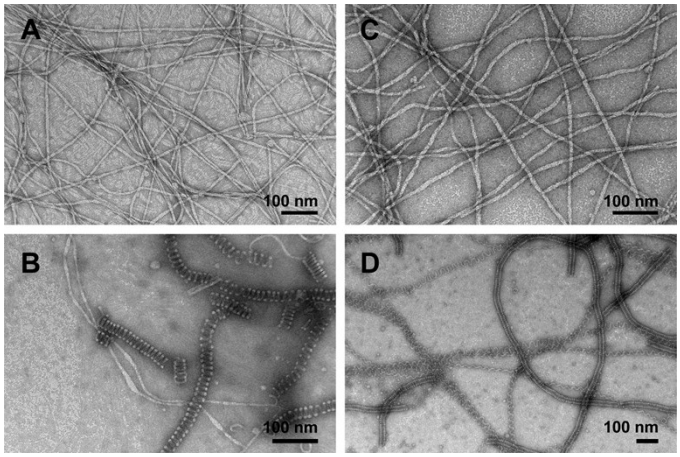

Fig. S3 Conventional TEM characterization illustrates the effect of salt concentration on the self-assembled morphology of APAs. In 10 mM PB: (A) $\mathbf{K_SNEK_S}$ assembled into nanoribbons; (C) $\mathbf{K_S}\boldsymbol{C'}\mathbf{EK_S}$ assembled into nanoribbons; In 100 mM PB: (B) $\mathbf{K_SNEK_S}$ assembled into primarily tight nanohelices with some nanoribbons; (D) $\mathbf{K_S}\boldsymbol{C'}\mathbf{EK_S}$ assembled into tight and loose nanohelices. All grids were stained with UA prior to imaging.

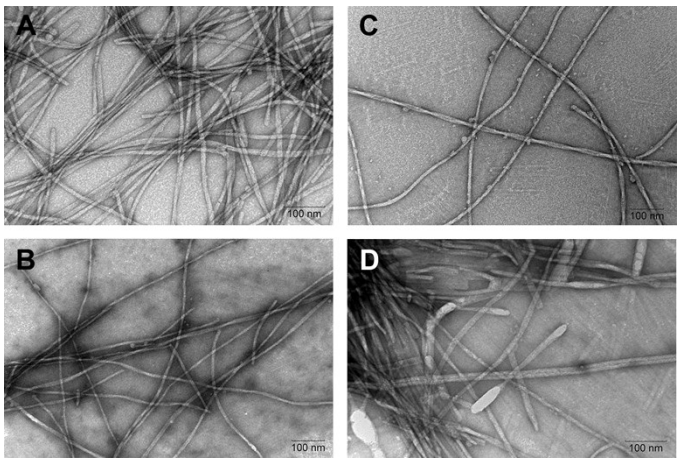

Fig. S4 Conventional TEM characterization illustrates that variation of salt concentration did not induce morphologic changes in the oxime-containing control APAs. (A, B) Nanoribbons formed by $\mathbf{K_ONEK_O}$ in aqueous solution; (C, D) Nanoribbons formed by $\mathbf{K_O}\boldsymbol{C'}\mathbf{EK_O}$ in aqueous solution; All grids were stained with UA prior to imaging. PB concentration was 10 mM for A and C and 100 mM for B and D.

Fluorescence spectroscopy:

Nile Red was used as a fluorescent probe to determine the critical aggregation concentration (CAC) of each APA. Specifically, 10 μL of a 50 μM solution of Nile Red in acetone was added to each vial and dried under vacuum. APAs in 10 mM PB solutions (300 μL, pH 7.4) with different concentrations were added to each vial and aged overnight. Fluorescence spectroscopy was performed on a Varian Cary Eclipse fluorescence spectrophotometer with a scanning speed of 200 nm min^{-1}, a 1 nm data pitch, an integration time of 0.1 sec, and 10 nm slits. The excitation wavelength was 550 nm, and emission was monitored from 570 to 720 nm. The CAC value was taken to be the intersection between the linear fits of the high and low concentration regimes.

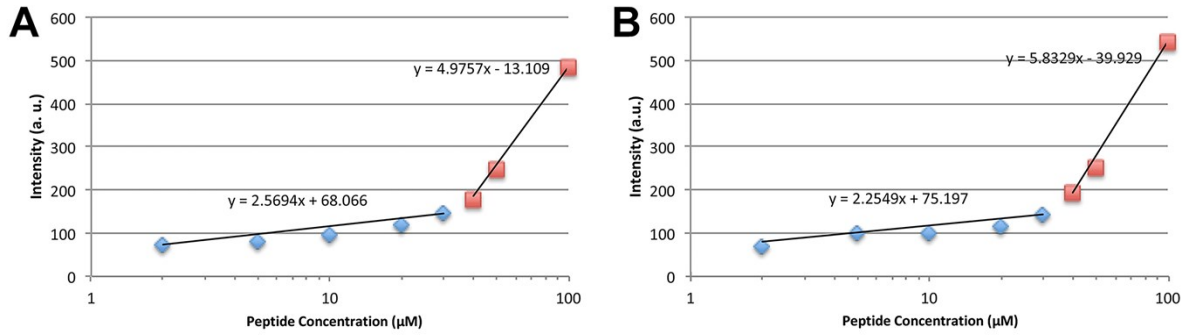

Fig. S5 Nile Red fluorescence intensity versus concentration plots of (A) $\mathbf{K_SNEK_S}$, and (B) $\mathbf{K_S}\boldsymbol{C'}\mathbf{EK_S}$ against concentration in 10 mM PB.

Table S1. CAC values of APAs calculated from Fig. S5

APA	CAC (μM)
K_SNEK_S	34
K_S*C'*EK_S	32

UV-vis spectroscopy:

UV-vis spectra of APAs from 190 to 400 nm were also recorded on a Jasco J-815 spectropolarimeter (JASCO, Easton, MD, USA) using a 1 mm path length quartz UV-Vis absorption cell (Thermo Fisher Scientific, Pittsburgh, PA, USA). The 100 μM samples diluted from 1 mM corresponding stock solutions in 10 mM PB or 100 mM PB (pH=7.4) were used in these measurements. A background spectrum of the solvent was acquired and subtracted from each sample spectrum.

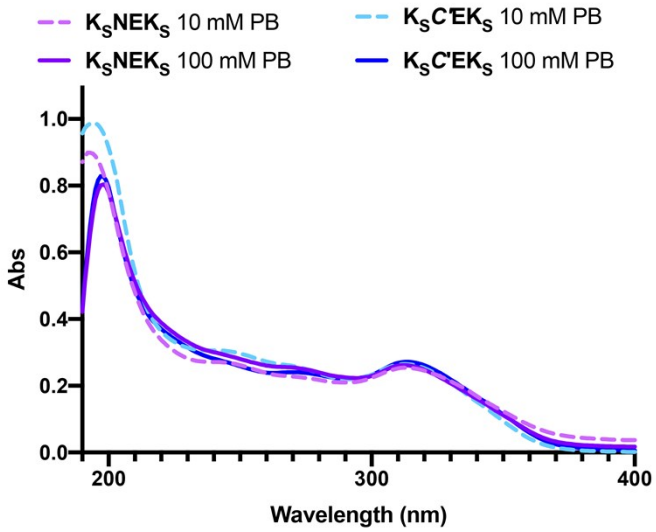

Fig. S6 UV-vis spectra of **K_SNEK_S** and **K_S*C'*EK_S** in 10 mM PB or 100 mM PB at a concentration of 100 μM.

IR spectroscopy:

IR spectra of all APAs were collected on a Nicolet 8700 FT-IR spectrometer equipped with an attenuated total reflectance (ATR) sampling accessory (Thermo Fisher Scientific). All APAs (1 mM) were first allowed to self-assemble for 10 h in 10 mM PB or 100 mM PB before lyophilization. Before IR measurements, lyophilized powders were rehydrated with D_2O, and all spectra were recorded as an average of 128 scans from 1800 to 1500 cm^{-1}. A background spectrum of a blank (10 mM or 100 mM PB in D_2O) was collected and subtracted from each sample spectrum. The traces were smoothed by the exponential smoothing method with a damping factor of 0.6 from Microsoft Excel (Version 16.35).

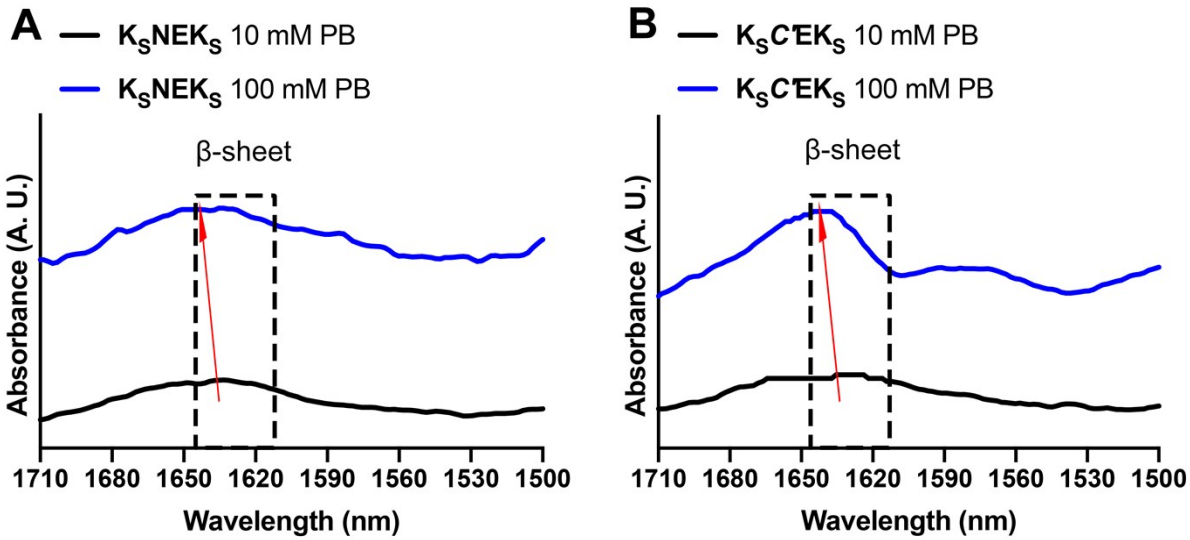

Fig. S7 FT-IR spectra of pre-assembled $\mathbf{K_SNEK_S}$ and $\mathbf{K_SC'EK_S}$ (1 mM) in 10 mM PB or 100 mM PB rehydrated in D_2O. Dashed boxes indicate the region for β-sheet amide-I bands; red arrows show redshift in absorbance peak upon increasing salt concentration.

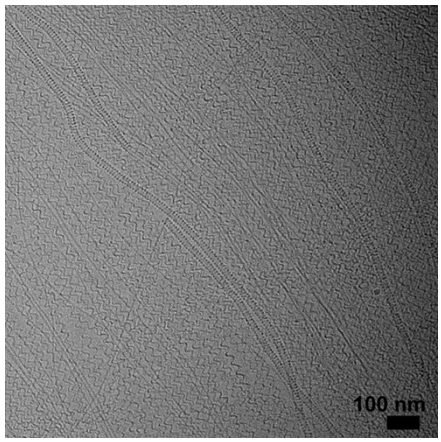

Fig. S8 Cryo-TEM image of $\mathbf{K_SC'EK_S}$ after incubation at room temperature for 14 days. Solution concentration: 1 mM $\mathbf{K_SC'EK_S}$ in 100 mM phosphate buffer (pH 7.4).

Coarse-grained (CG) model of K_SNEK_S:

We carried out CG simulations using the MARTINI force-field (FF) because it has been successfully used in the study of the self-assembly of peptide amphiphiles (PAs), lipid bilayers, and other biomolecules.[2-4] It uses a 4:1 mapping scheme where four heavy atoms and the hydrogens attached to these heavy atoms are combined together to form a CG bead. These beads are assigned a polar or non-polar type based on the hydrophilicity and hydrophobicity of the heavy atoms. The water molecules were treated explicitly as P4 beads along with 10 % anti freezing particles, BP4. Each P4 bead of water represented four atomistic water molecules. In this study, the CG model of **K_SNEK_S** was built as shown in Fig. S9. The oligoamide backbone of the APA sequence was represented by four P5 beads, attached with one N0E bead (representing the Asn side chain), one QAE bead (Glu side chain) and one P5N bead as side groups. Note that the QAE bead is kept uncharged or charged neutral, although it is a charged bead in the original MARTINI FF. The SATO group contains two benzene rings comprised of three SC4F beads in each, two P5N, and one C3K beads. All the beads are charge neutral.

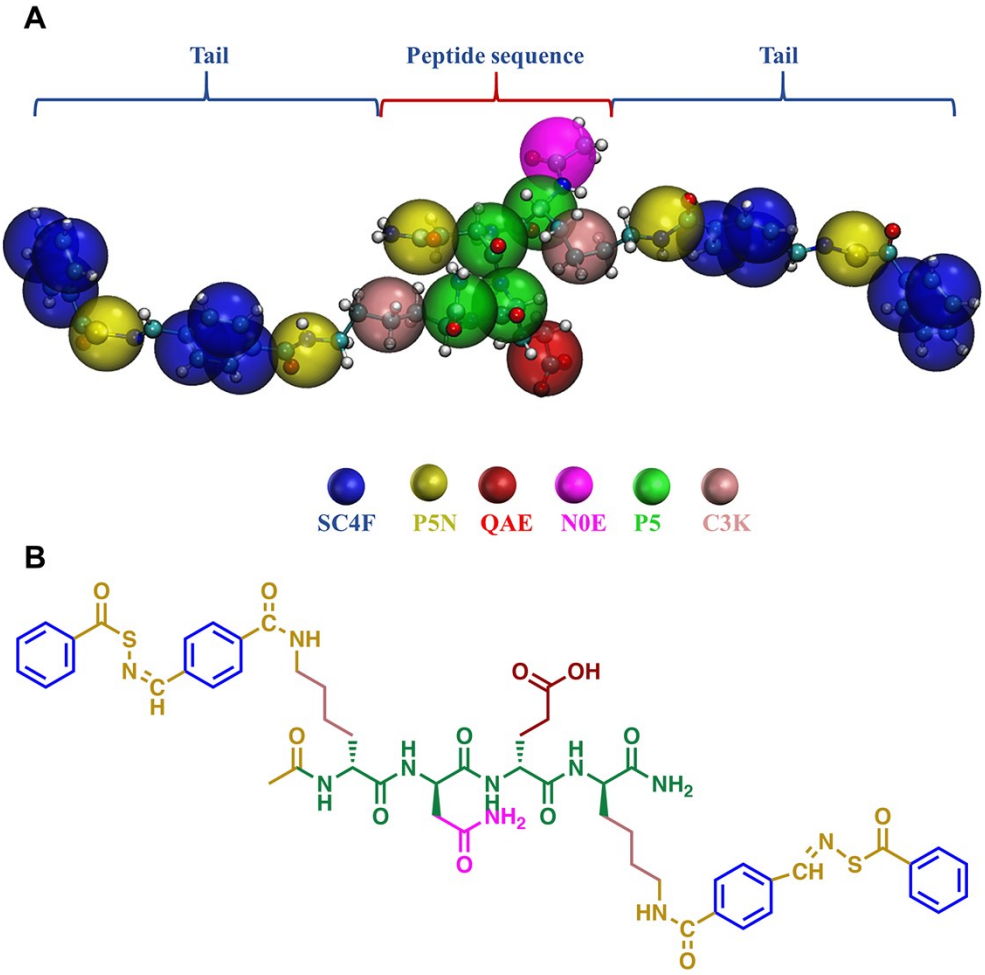

Fig. S9 (A) The mapping scheme of the MARTINI **K_SNEK_S** model and (B) its chemical structure. The color of the functional groups from (B) are the same as those of the CG beads shown in (A).

Harmonic bond and cosine-based harmonic angle potentials were used to represent the bonded interactions, while the nonbonded interactions were described by the 12-6 Lennard-Jones (LJ) function (Equation S1).

$$E_{lj} = 4E_{ij}\left[\left(\frac{\sigma_{ij}}{r_{ij}}\right)^{12} - \left(\frac{\sigma_{ij}}{r_{ij}}\right)^{6}\right] \quad \text{..... Equation S1}$$

Where ε_{ij} is the depth of the potential well and represents the strength of interactions between two beads i and j, σ_{ij} is the finite distance at which the inter-particle potential is zero, and r_{ij} is the distance between two beads. Parameters for the two selected bead types QAE and SC4F beads with themselves and with water beads P4 are shown in Table S2.

Simulations were performed by using the NAMD GPU package.[5] 150 APA molecules were solvated in ~32500 CG water molecules (10% were antifreezing beads). All simulations were carried out in the isothermal-isobaric (NPT) ensemble. The temperature was kept constant at 300 K, and the pressure was kept at 1 bar by using the Langevin thermostat and barostat.[6-8] The barostat oscillation time scale for the Langevin piston was kept at 1 ps. The piston decay specifying the barostat damping time scale for the Langevin piston method was kept at 1 ps. The Verlet-velocity algorithm was used to integrate the equations of motion with a timestep of 25 fs. The pair list distance for storing neighbor beads of a given one was set to be 14 Å. The beads separated by two bonds interacted with nonbonded interactions, and the cutoff distance for calculating nonbonded interactions was 12 Å. A switch function was applied at 9 Å to smooth the truncation of the van der Waals interactions. Trajectories of the last 150 ns were used for calculating RDFs and SASA.[9-12]

Table S2. Parameters in the LJ potential for selected bead pairs in the MARTINI $\mathbf{K_SNEK_S}$ model.

	ε (kcal/mol)	σ (Å)
SC4F-SC4F[a]	0.62739	4.3
QAE-QAE[a]	1.19503	4.7
SC4F-SC4F[b]	0.8	4.3
QAE-QAE[b]	1.19503	4.7
SC4F-SC4F[c]	1.0	4.3
QAE-QAE[c]	0.6	4.7
QAE-P4	1.33843	4.7
SC4F-P4	0.645315	4.7

[a] Interaction parameters that led to the formation of a nanoribbon with a width and thickness

of ~ 15 nm and ~ 4.5 nm, respectively.
[b] Interaction parameters that led to the formation of a nanoribbon with a width and thickness of ~ 7.5 nm and ~ 4.5 nm, respectively.
[c] Interaction parameters that led to the formation of a nanohelix.

Table S3. Scaled parameters in the LJ potential for hydrophilic bead pairs in the MARTINI $\mathbf{K_SNEK_S}$ model. The hydrophilic beads selected here were P5 in the neighborhood of QAE bead of $\mathbf{K_SNEK_S}$. Parameters for all other beads not listed here were used as they are from the MARTINI FF.

	ε (kcal/mol)	σ (Å)
Simulation 1		
P5-P5	0.672	4.7
SC4F-SC4F	1.0	4.3
QAE-QAE	0.6	4.7
Simulation 2		
P5-P5	1.0707	4.7
SC4F-SC4F	1.0	4.3
QAE-QAE	0.956	4.7

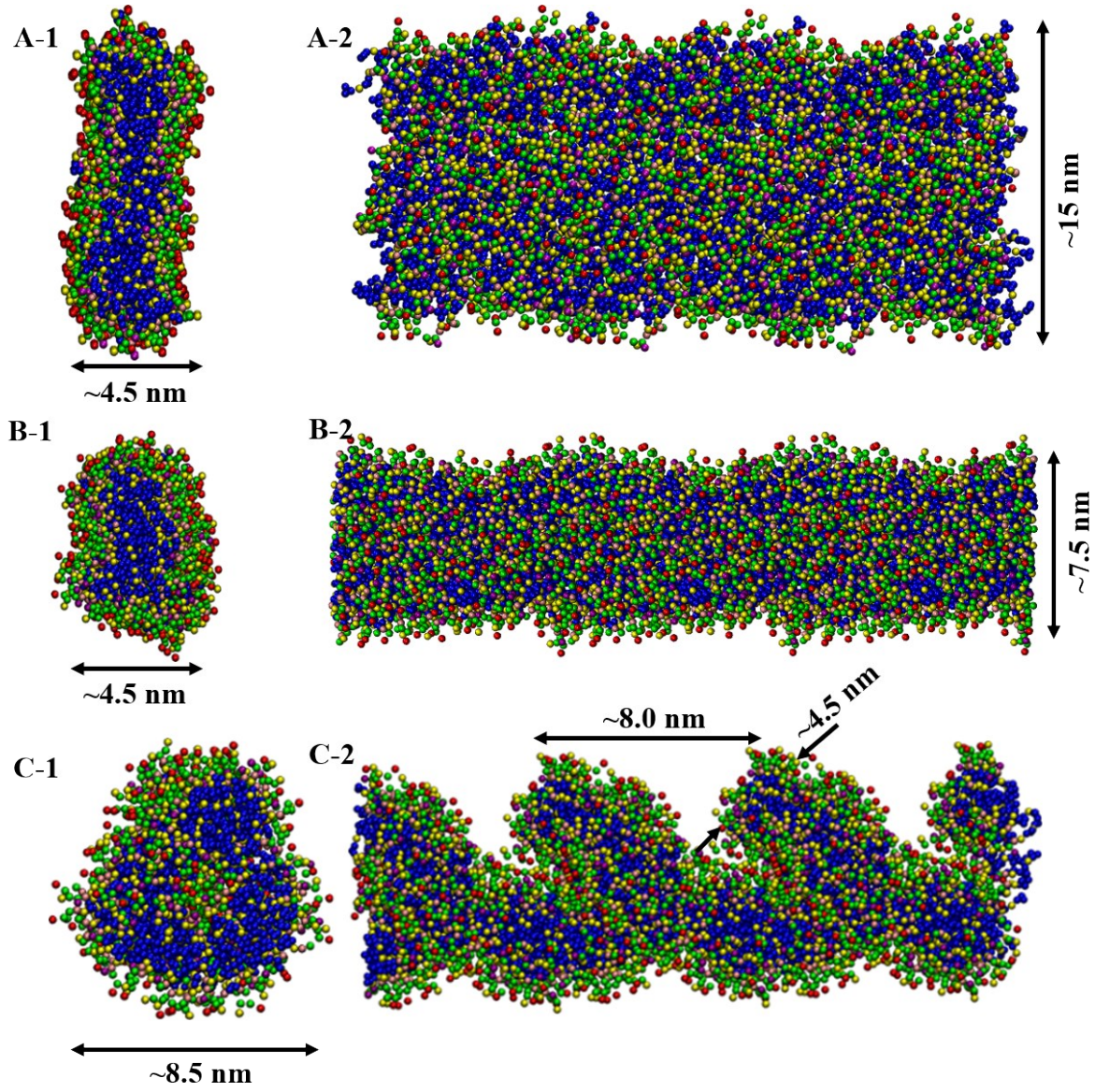

Fig. S10 The enlarged snapshots of nanoribbon and nanohelices at ~ 15 μs of the CG MD simulations. (A) Nanoribbons with a width of ~ 15 nm, ε[SC4F-SC4F] = 0.62739 kcal/mol, ε[QAE-QAE] = 1.19503 kcal/mol; (B) Nanoribbons with a width of ~ 7.5 nm, ε[SC4F-SC4F] = 0.8 kcal/mol, ε[QAE-QAE] = 1.19503 kcal/mol; and (C) Nanohelices, ε[SC4F-SC4F] = 1.0 kcal/mol, ε[QAE-QAE] = 0.6 kcal/mol; (1): side view, (2): top view. Color scheme can be found in Fig. S9.

Radial distribution functions:

As stated in the manuscript, to obtain the nanohelices, interactions between the hydrophobic SC4F beads with themselves were increased to 1.0 kcal/mol from 0.8 kcal/mol in the nanoribbon with a width of ~7.5 nm. In addition, we also decreased the interactions between the hydrophilic QAE beads with themselves to 0.6 kcal/mol in a nanohelix from ~1.19 kcal/mol in a nanoribbon. In both cases, interactions of SC4F-P4 and QAE-P4 were 0.645315 kcal/mol

and 1.33843 kcal/mol, respectively. To understand the effect of the change in the interactions on the local structure of APAs in nanohelices and nanoribbons, we calculated the RDFs of SC4F-SC4F and QAE-QAE bead pairs. As can be seen in Fig. S11A, the height of the first peak (at ~4.6 Å) in the RDF of the SC4F-SC4F bead pair is higher in the nanohelix than in the nanoribbon. This indicates that the ordering of SC4F beads is more prominent in the nanohelices than in the nanoribbons. In the case of the RDF of the QAE-QAE bead pair (Fig. S11B), the height of the first peak (at ~5.0 Å) decreased significantly in the nanohelix compared to the nanoribbon. This suggests that QAE bead pairs are less ordered in the nanohelix than in the nanoribbon.

Solvent accessible surface area (SASA) is the surface area of a given molecule that is accessible to solvent.[9] The built-in "measure sasa" command in VMD was used to obtain SASA values for the nanohelices and nanoribbons.[12] The algorithm for calculating SASA was first developed by Lee and Richards, which involved the extension of the van der Waals radius for each atom by 1.4 Å (the radius of a polar solvent probe) and the calculation of the surface area of these expanded-radius atoms.[10, 11]

To understand the effect of changing in the interactions between hydrophilic QAE beads with themselves on the structure of water, we calculated the RDF for QAE-P4 bead pairs in both the nanohelix and nanoribbon. It can be seen in Fig. S11C that the RDFs of QAE-P4 bead pairs in a nanohelix and in a nanoribbon are very similar.

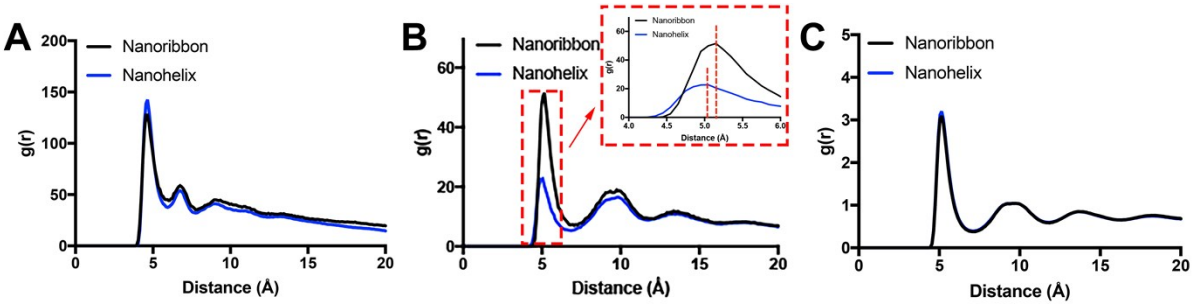

Fig. S11 The RDFs of beads pairs: (A) SC4F-SC4F (B) QAE-QAE, and (C) QAE-P4. Inset in the top right corner of panels B shows the zoomed-in plot outlined by the dashed red rectangle.

Hydrolysis experiments:

Hydrolysis experiments were carried out in 1.5 mL centrifuge tubes. 1 mM stock solutions of $\mathbf{K_SNEK_S}$ in 10 mM or 100 mM PB solution (pH 7.4) were prepared by direct dissolution of the lyophilized powders. At various time intervals, 20 μL of solution was withdrawn and diluted to 200 μL by 10 mM or 100 mM PB. The UV-vis spectra of APAs from 200 nm to 400 nm were recorded on a Varian Cary 100 UV-vis spectrophotometer (Agilent Technologies, Santa Clara, CA) using a 1 cm path length quartz UV-Vis absorption cell (Thermo Fisher Scientific, Pittsburgh, PA, USA). A background spectrum of the solvent was acquired and subtracted from each sample spectrum. The data were then plotted as SATO percentage remaining versus time.

$$SATO\ remaining\ (\%) = \frac{Abs_{ti}}{Abs_{t0}} \times 100\%$$ ..... Equation S2

Where Abs_{ti} is absorbance of the SATO λ_{max} (320 nm) at each time interval, and Abs_{t0} is the initial absorbance of the SATO λ_{max} (320 nm).

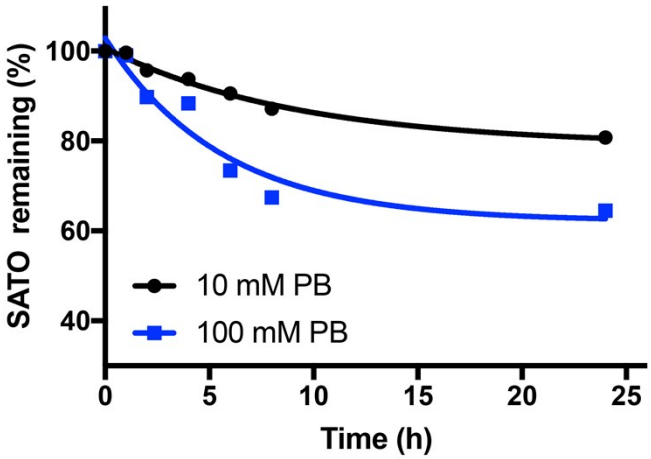

Fig. S12 Hydrolysis experiments of $\mathbf{K_SNEK_S}$ in 10 mM or 100 mM PB as monitored by UV-vis spectra.

Ionic conductivity measurements:

Ionic conductivity measurements were carried out on a conductivity meter (HANNA instruments, Smithfield, RI) at rt. Pure buffer and buffer containing unassembled APAs or nanostructures were used in the measurements. Buffer containing unassembled APAs or nanostructures was prepared by mixing 1 mL of 1 mg/mL $\mathbf{K_SNEK_S}$ in PB with 19 mL of corresponding PB buffer, with vortexing for 1 min prior to measurements. Ionic conductivity measurements of poly(sodium 4-styrene-sulfonate), poly(acrylic acid), alginic acid, and deoxyribonucleic acid from herring sperm were carried out in the same way.

Table S4. Conductivity increases of $\mathbf{K_SNEK_S}$, common charged biomolecules, and polymers in PB with different salt concentrations.

	Concentration of anionic group (mM)	Conductivity increase (x 10^2 μS/cm)	
		10 mM PB	100 mM PB
$\mathbf{K_SNEK_S}$	1	0.4	8.6
poly(acrylic acid)	14	0.4	1
poly(sodium 4-styrene-sulfonate)	5	0.17	0.6
alginic acid	6	0.33	0.7
deoxyribonucleic acid from herring sperm (DNA)	3	0.13	1.7

Thickness measurements of twisted nanoribbons from cryo-TEM images

The thickness of twisted nanoribbons was measured according to a previous report.[13] In brief, the twists of nanoribbons ($n \geq 50$) from different cryo-TEM images were measured by ImageJ (1.52k) by measuring the thickness at the narrowest part of the twist (Fig. S13). The mean thickness was determined by averaging all the obtained values.

Fig. S13 Cartoon of a twisted nanoribbon pointing out how thickness was measured.

References

1. J. C. Foster, C. R. Powell, S. C. Radzinski and J. B. Matson, S-aroylthiooximes: a facile route to hydrogen sulfide releasing compounds with structure-dependent release kinetics. *Org. Lett.*, 2014, **16**, 1558-1561.
2. S. A. Deshmukh, L. A. Solomon, G. Kamath, H. C. Fry and S. K. R. S. Sankaranarayanan, Water ordering controls the dynamic equilibrium of micelle-fibre formation in self-assembly of peptide amphiphiles. *Nat. Commun.*, 2016, **7**, 12367.
3. O. S. Lee, V. Cho and G. C. Schatz, Modeling the self-assembly of peptide amphiphiles into fibers using coarse-grained molecular dynamics. *Nano Lett*, 2012, **12**, 4907-4913.
4. S. Mushnoori, K. Schmidt, V. Nanda and M. Dutt, Designing phenylalanine-based hybrid biological materials: controlling morphology via molecular composition. *Org. Biomol. Chem.*, 2018, **16**, 2499-2507.
5. J. C. Phillips, R. Braun, W. Wang, J. Gumbart, E. Tajkhorshid, E. Villa, C. Chipot, R. D. Skeel, L. Kale and K. Schulten, Scalable molecular dynamics with NAMD. *J. Comput. Chem.*, 2005, **26**, 1781-1802.
6. B. Mishra and T. Schlick, The notion of error in Langevin dynamics .1. Linear analysis. *J. Chem. Phys.*, 1996, **105**, 299-318.
7. S. E. Feller, Y. H. Zhang, R. W. Pastor and B. R. Brooks, Constant-pressure molecular-dynamics simulation - the Langevin Piston Method. *J. Chem. Phys.*, 1995, **103**, 4613-4621.
8. W. Wang and R. D. Skeel, Analysis of a few numerical integration methods for the Langevin equation. *Mol. Phys.*, 2003, **101**, 2149-2156.
9. E. Durham, B. Dorr, N. Woetzel, R. Staritzbichler and J. Meiler, Solvent accessible surface area approximations for rapid and accurate protein structure prediction. *J. Mol. Model.*, 2009, **15**, 1093-1108.
10. B. Lee and F. M. Richards, The interpretation of protein structures: Estimation of static accessibility. *J. Mol. Biol.*, 1971, **55**, 379-IN374.

11. A. Shrake and J. A. Rupley, Environment and exposure to solvent of protein atoms - Lysozyme and insulin. *J. Mol. Biol.*, 1973, **79**, 351-371.
12. W. Humphrey, A. Dalke and K. Schulten, VMD: Visual molecular dynamics. *J. Mol. Graph.*, 1996, **14**, 33-38.
13. Y. A. Lin, Y. C. Ou, A. G. Cheetham and H. G. Cui, Supramolecular polymers formed by ABC miktoarm star peptides. *ACS Macro Lett.*, 2013, **2**, 1088-1094.